

Merging black holes with Cauchy-characteristic matching: Computation of late-time tails

Sizheng Ma ^{1,*} Mark A. Scheel ² Jordan Moxon ² Kyle C. Nelli ² Nils Deppe ^{3,4,5} Lawrence E. Kidder ⁵ William Throwe ⁵ and Nils L. Vu ²

¹*Perimeter Institute for Theoretical Physics, Waterloo, ON N2L2Y5, Canada*

²*TAPIR 350-17, California Institute of Technology, 1200 E California Boulevard, Pasadena, CA 91125, USA*

³*Laboratory for Elementary Particle Physics, Cornell University, Ithaca, New York 14853, USA*

⁴*Department of Physics, Cornell University, Ithaca, New York 14853, USA*

⁵*Cornell Center for Astrophysics and Planetary Science, Cornell University, Ithaca, New York 14853, USA*

(Dated: December 11, 2024)

We present successful evolutions of binary black hole mergers using a novel numerical-relativity technique known as Cauchy-characteristic matching (CCM). This approach eliminates systematic errors associated with boundary conditions, effectively extending the computational domain to infinity. As an important application, we use CCM to resolve a late-time power-law tail in the gravitational wave from a head-on collision, and show that the tail is highly suppressed in a quasi-circular binary. Our results for the two extreme cases (orbital eccentricity = 0, 1) support the fact that tails increase with orbital eccentricity. Therefore, CCM paves the way for a detailed understanding of tails in eccentric systems. For the head-on case, we find that the tail behavior is consistent with predictions in the intermediate regime from black hole linear perturbation theory. However, we also raise the possibility that the power-law tail could be generated nonlinearly by quasinormal modes. The nonlinear contribution is expected to decay slower than predicted by Price’s law, potentially dominating the signal at late times. If confirmed as nonlinear, this would be an example where nonlinearity prevails over linearity in the late-time regime of black hole dynamics.

Introduction. — Numerical relativity (NR) remains, to date, the only *ab initio* method to produce gravitational wave (GW) waveforms from binary black hole (BBH) mergers. However, these waveforms could be contaminated by systematic errors in NR, leading to false alarms of deviations from general relativity, especially for data analysis in third-generation detectors. A major source of such systematic errors is boundary conditions [1, 2], which approximate the underlying physical system. Therefore, for future GW astronomy, it would be beneficial to design a NR system that extends to infinity, thereby eliminating contamination from boundary conditions.

Cauchy-characteristic matching (CCM) [3] offers a promising path toward this goal¹. This method adopts two complementary formalisms to handle different regions of spacetime: the Cauchy formalism for near zone [6–8] and the characteristic formalism [3, 9–15] for wave zone. The two systems intersect at a 3D timelike worldtube, where each provides *exact* boundary conditions for the other. By evolving simultaneously, the matched framework effectively constructs an infinite computational domain and generates exact solutions of Einstein’s equations across both the near and wave zones.

The two key components of CCM — the Cauchy and characteristic formalisms — have been well-developed in the past, leading to an accurate GW extraction method known as Cauchy-characteristic evolution (CCE) [16, 17].

CCE has been used to investigate memory effects and Bondi-van der Burg-Metzner-Sachs (BMS) symmetry of BBH systems [17]. However, the study of CCM is still at a very preliminary stage.

Recently, we developed a fully relativistic algorithm to perform CCM for *any* numerical spacetime [18] (hereafter Paper I). The method is free of approximations and has been tested on various simple yet nontrivial systems. In this paper, we present the successful application of the algorithm to BBH mergers, along with a late-time tail uncovered through the method.

Throughout this paper we use Latin indices i, j, k, \dots to denote 3D spatial components and Greek indices μ, ν, \dots for 4D spacetime components. The initial ADM mass of binary systems is denoted by M .

Summary of CCM. — Our Cauchy evolution adopts the Generalized Harmonic (GH) formalism described in [19], which formulates the vacuum Einstein equations as first-order symmetric hyperbolic partial differential equations. This system evolves fifty variables: the metric $g_{\mu\nu}$, its normal-time derivative $\Pi_{\mu\nu} = \alpha^{-1}(\beta^i \partial_i g_{\mu\nu} - \partial_t g_{\mu\nu})$, and spatial derivative $\Phi_{i\mu\nu} = \partial_i g_{\mu\nu}$, where α and β^i are the lapse and shift, respectively.

At the outer boundary, boundary conditions are imposed on forty incoming characteristic fields, including [19, 20]

$$\begin{aligned} u_{\mu\nu}^0 &= g_{\mu\nu}, & u_{i\mu\nu}^2 &= P_i^k \Phi_{k\mu\nu}, \\ u_{\mu\nu}^1 &= \Pi_{\mu\nu} - s^i \Phi_{i\mu\nu} - \gamma_2 \psi_{\mu\nu}, \end{aligned} \tag{1}$$

where s^i is the outward unit normal vector of the boundary, $P_i^k = \delta_i^k - s_i s^k$ is the projection operator, and γ_2 is

¹ An alternative approach is to adopt hyperboloidal slicing, see [4, 5] and references therein.

a constraint damping parameter. As noted in [19], the boundary conditions can be divided into three subsets: constraint, physical, and gauge.

In the constraint subset, the normal derivatives of $u_{\mu\nu}^0$, $u_{i\mu\nu}^2$, and four components of $u_{\mu\nu}^{1-}$ are related to incoming constraint modes [see Eq. (59)-(61) in [19]]. Imposing constraint-preserving conditions yields Neumann conditions on these thirty-four variables. Thus, CCM is unnecessary here, as manual constraint injection lacks physical motivation and may cause numerical instability.

The physical subset involves two other components of $u_{\mu\nu}^{1-}$ and encodes information about backscattered GWs. According to Eq. (66) and (67) in [19] and Eq. (2.12) in Paper I, these degrees of freedom are related to the Weyl scalar Ψ_0 , corresponding to the two polarizations of the backscattered radiation. Setting boundary conditions for this subset requires precisely modeling the backscattered waves outside the Cauchy domain, which was achieved in Paper I. Since the two components of $u_{\mu\nu}^{1-}$ are represented on the Cauchy grid with the Cauchy tetrad, careful gauge and tetrad transformations are necessary before matching. We have verified that neglecting these transformations can cause instability in CCM simulations. In Paper I, we developed a general method for handling these transformations in any numerical spacetime.

In the wave zone, a numerical spacetime can be approximated as a perturbed Schwarzschild BH, allowing the use of the Regge-Wheeler-Zerilli (RWZ) formalism to estimate the evolution of Ψ_0 . This approach leads to “higher order boundary conditions” (HOBCs) [21–24] that absorb outgoing multipolar radiation up to a specified angular momentum order L . HOBCs have three major approximations: (1) nonlinear effects are omitted; (2) a truncation order L must be chosen; (3) the RWZ formalism is applied in the BH’s rest frame, usually different from the Cauchy frame. Although Ψ_0 is an invariant at the linear level, it is still represented on the Cauchy grid and thus the angular coordinate mismatch at the boundary between the rest and Cauchy frames can cause mode mixing. Our CCM implementation relaxes these approximations, effectively providing an infinite-order ($L = \infty$) nonlinear boundary condition. When linearized around a Schwarzschild background, the CCM algorithm should reproduce HOBCs.

Finally, the gauge subset determines the remaining four components of $u_{\mu\nu}^{1-}$. It implicitly sets the boundary conditions for the GH gauge [23, 25–27]

$$\square x^\mu = H^\mu, \quad (2)$$

where \square is the d’Alembert operator, and H^μ are freely specifiable gauge source functions, here chosen as the Damped Harmonic gauge [28]. As we will show below, while this subset controls the dynamics of the Cauchy grids, it *does not* affect GWs once transformed into the Bondi-Sachs frame (modulo BMS transformations [29, 30]), which represents inertial observers at future null

infinity. Therefore, for waveform modeling, CCM is not required for this subset.

However, this does not mean that the gauge subset is unimportant in numerical simulations. As noted in [31], poorly chosen gauge boundary conditions can cause an exponential drift of a binary’s center of mass over a long timescale. Although this drift is a gauge effect, it can lead to numerical challenges and increase computational costs. In the following discussions, we mainly adopt the Sommerfeld boundary condition for the subset [26].

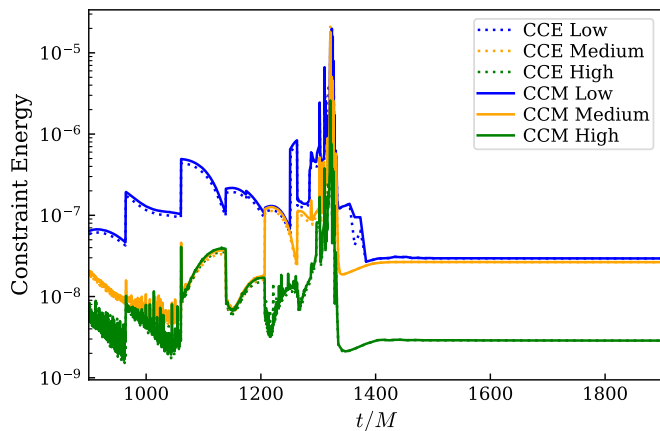
To summarize, the primary (and probably the only) task of CCM is to model backscattered GWs. In strong-gravity regions, it is well known that there is no canonical definition for local physical quantities like gravitational energy. This suggests that CCM could naturally be a cumbersome procedure, requiring the consideration of all dynamical variables. However, the GH formalism simplifies this significantly by providing a framework to isolate the relevant subset of variables. By focusing exclusively on this reduced subset, along with the tricks described in Paper I, CCM becomes computationally manageable.

SpEC-SPECTRE CCM system.— Our spectral characteristic evolution [13–15], together with the CCM system in Paper I, is built in SpECTRE [32]. However, since BBH mergers have only recently become feasible in SpECTRE [33], we use the more mature NR code, SpEC [34], to develop a SpEC-SPECTRE hybrid CCM system. This design links the SpECTRE characteristic module to SpEC’s executable, enabling SpEC to invoke SpECTRE functions as needed throughout the simulation. Specifically, we adopt SpEC’s time stepper, chosen as the fifth-order Dormand-Prince integrator, to evolve both Cauchy and characteristic variables. The SpECTRE module is used only for evaluating the right-hand sides of the characteristic equations and computing quantities necessary for CCM.

Our CCM system can stably evolve BBH mergers without requiring fine-tuning of constraint damping parameters. We use common values as in other SXS simulations, see Eqs. (53), (54), and Table 2 of [33]. Simulations are run at three resolutions (“Low”, “Medium”, and “High”). The Cauchy resolution is set by specifying numerical error tolerances for the adaptive mesh refinement algorithm [35], while the characteristic resolution is controlled by the number of grid points in angular and radial directions.

The SpEC initial data solver generates Cauchy initial data through the Extended Conformal Thin Sandwich formulation [36–38]. Superposed harmonic-Kerr [39] data is adopted to reduce junk radiation. While Sec. II E of [15] lists various methods to construct characteristic initial data, it omits details of SpECTRE’s default algorithm, which we summarize in the Supplementary Material.

Head-on collision.— We first consider a head-on collision of two equal-mass, nonspinning BHs. Their initial separation is set to $110M$. The outer boundary and the time-like worldtube for CCM are placed at a radius of $650M$ from the center of mass. Since the common horizon



(a) Cauchy GH constraint energy.

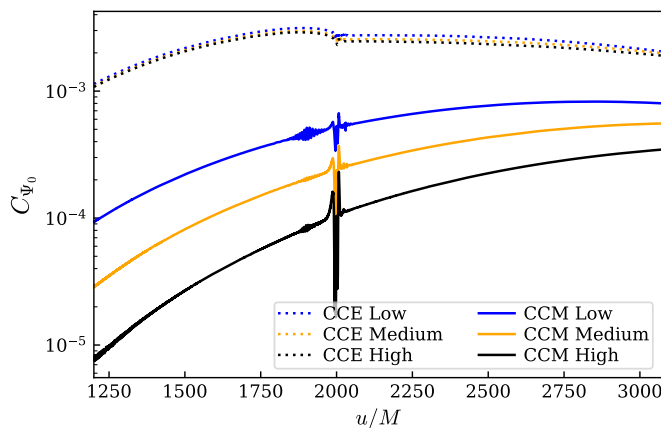
(b) Bianchi identity for Ψ_0 in the Bondi frame.

Figure 1. Top panel: The L^2 -norm of the Cauchy GH constraint energy using CCM at three resolutions, shown as a function of Cauchy time t . Bottom panel: The violation of the Bianchi identity for Ψ_0 at future null infinity [Eq. (3)], using CCE (dotted curves) and CCM (solid curves). The retarded time u is used.

forms at $t = 1323.7M$, the interior dynamics are in causal contact with the outer boundary. Consequently, boundary conditions will impact the evolution. The remnant is a Schwarzschild BH with a mass of $0.99712M$.

Figure 1a shows the L^2 -norm of the Cauchy GH constraint energy [Eq. (53) in [19]] for the CCM simulations at three resolutions (solid curves). The constraints converge with resolution and become constant once the system settles down. No instabilities are observed. A comparison with a standard Cauchy evolution (without matching but under otherwise identical conditions) shows that CCM does not significantly alter the constraint energy (dotted curves), in agreement with Paper I.

In a Bondi frame, Einstein’s equations and the Bianchi identities link various waveform quantities. For example, the Weyl scalars $\Psi_{0,1,2}$ and the strain h are connected as

follows, e.g., [40, 41]

$$\dot{\Psi}_0 = -\frac{1}{2}\bar{\partial}\Psi_1 + \frac{3}{4}\bar{h}\Psi_2, \quad (3)$$

where the dot denotes the retarded-time derivative. Since CCM computes these quantities independently at future null infinity, this relation can be used to assess the accuracy of CCM and identify any violations of the Bondi gauge. Figure 1b shows the L^2 -norm of the violation, which converges with resolution. In contrast, waveforms extracted using CCE from standard Cauchy evolutions without matching (dotted lines) show much poorer convergence. Besides Eq. (3), there are five more relations involving other Weyl scalars, the strain, and the News. CCM can consistently improve the constraints by roughly an order of magnitude, except for those already below 10^{-6} . This is shown in the Supplementary Material.

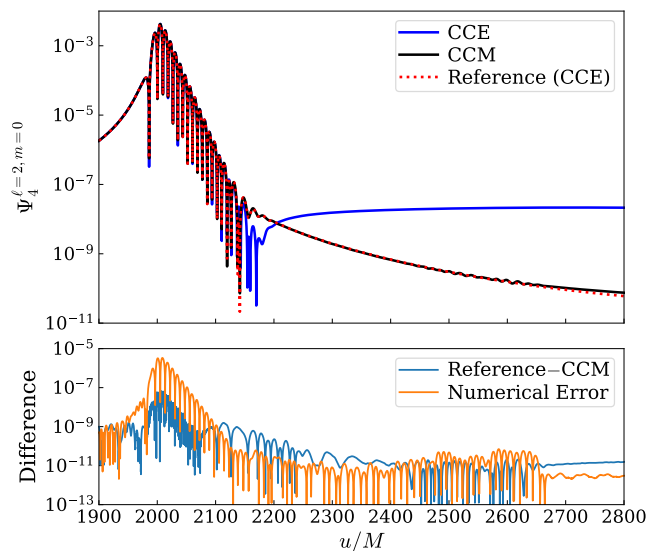


Figure 2. Top panel: $\Psi_4^{\ell=2,m=0}$ emitted from a head-on BBH collision, simulated using CCE (blue) and CCM (black). The “High” resolution is used. They are compared to a reference system (red), whose outer boundary remains causally disconnected from the binary throughout the simulation. Bottom panel: The difference between the reference and CCM results (blue), along with an estimate of the numerical error (orange).

The black curve in Fig. 2 shows the evolution of the ($\ell = 2, m = 0$) harmonic of Ψ_4 at future null infinity, computed at the highest resolution. It is compared to the extraction without matching (in blue). We focus on Ψ_4 because its functional form is unaffected by supertranslations, see Eq. (17e) in [42], thus avoiding a DC offset from memory effects. Significant differences are evident at late times. To validate the CCM simulation, we conduct a reference simulation without CCM, whose outer boundary, positioned at 6000, remains causally disconnected from the system. This reference result (in red) nearly overlaps the black curve. The lower panel of Fig. 2 shows the difference between the reference and CCM results (in blue),

together with an estimate of numerical error obtained by taking the difference between two adjacent resolutions (“Medium” and “High”). The comparable differences confirm that CCM accurately models backscattered waves and converges to the exact infinite domain problem.

Both the reference and CCM results reveal a non-oscillatory “tail” following the quasinormal-mode (QNM) ringing, starting at $u \sim 160M$ after the peak of $\Psi_4^{\ell=2,m=0}$. A more detailed discussion of this tail behavior will be provided in the next section.

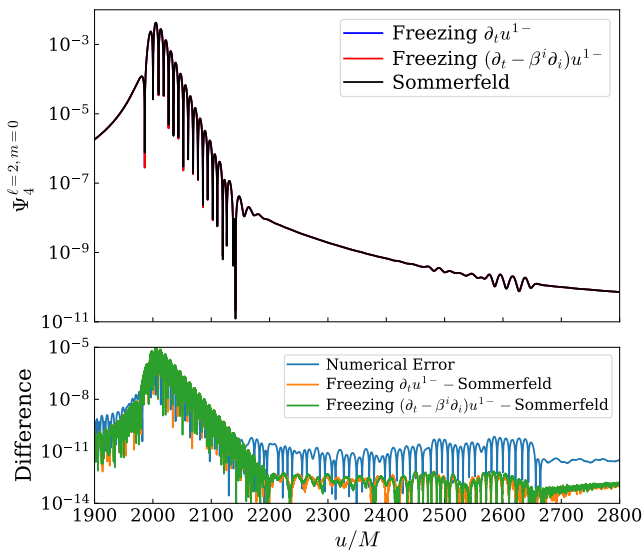


Figure 3. Top panel: Comparison between different gauge boundary conditions, including (1) the Sommerfeld condition (black), (2) freezing the gauge projection of $\partial_t u_{\mu\nu}^{1-}$ (blue), and (3) freezing the gauge projection of $(\partial_t - \beta^i \partial_i) u_{\mu\nu}^{1-}$ (red). $\Psi_4^{\ell=2,m=0}$ emitted from a head-on BBH collision is shown, simulated using CCM at the “Medium” resolution. Bottom panel: The differences between the results (in orange and green), along with an estimate of the numerical error (blue).

Finally, we investigate the impact of the gauge boundary condition. Besides the Sommerfeld condition [Eq. (25) in [26]], we also choose to freeze (i) the gauge projection of $\partial_t u_{\mu\nu}^{1-}$, i.e. Eq. (14) in [26], and (ii) the gauge projection of $(\partial_t - \beta^i \partial_i) u_{\mu\nu}^{1-}$. Their results at the “Medium” resolution are shown in Fig. 3. The bottom panel indicates that the differences among these choices are on par with the numerical error, supporting that gauge boundary conditions do not impact GWs.

Tail analysis with rational filters.— Tail analysis could be affected by the presence of QNMs. Although pushing the analysis window to later times can mitigate the issue, it also causes unnecessary signal loss, especially for NR waveforms. Additionally, the tail could already exist beneath the QNM ringing at earlier times, making this approach overlook its early-time contribution.

We adopt QNM rational filters [43–45] and the PYTHON package `qnm_filter` [46] to address this issue, which

enable mode removal without fitting. We first apply the Fourier-analysis method from Sec. III B of [47] to identify QNMs. We find $\omega_{\ell=2,m=0,n=0,1}$, a quadratic QNM $2\omega_{200}$, and their mirrors. These are then filtered out from the ringdown regime. As noted in Sec. II B and Fig. 3 of [43], these filters introduce a backward time shift in a power-law tail, with an analytical expression provided in Eq. (16) therein. We have verified that this formula accurately describes our case. Therefore, we apply this formula to adjust for the time shift in the following analysis.

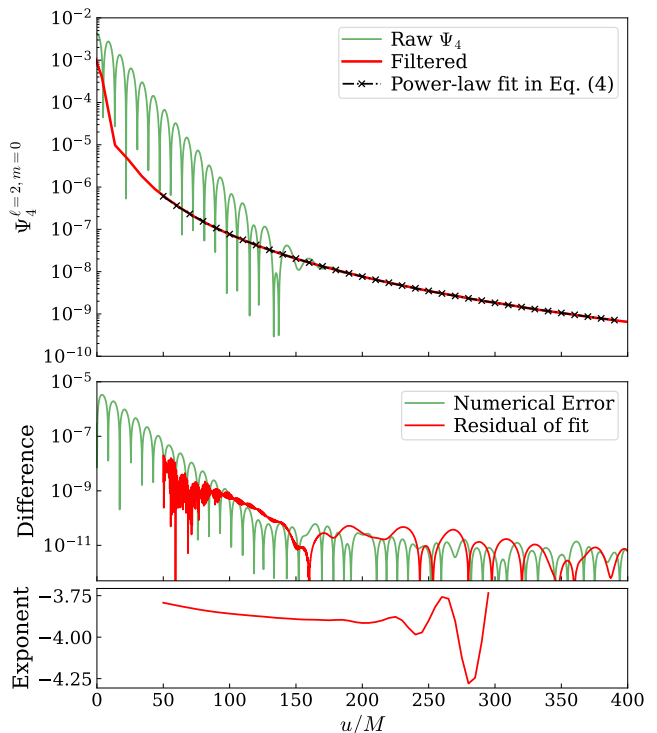


Figure 4. Top panel: The raw (green) and filtered (red) $\Psi_4^{\ell=2,m=0}$ simulated using CCM at the “High” resolution. The power-law fit in Eq. (4) is shown in black (marked with crosses). Middle panel: The residual of the power-law fit (red), compared to the numerical error (green). Bottom panel: The fitted power-law exponent for the filtered $\Psi_4^{\ell=2,m=0}$ in the time window $[u_{\text{start}}, 400M]$, with u_{start} ranging from $50M$ to $300M$.

The red curve in the top panel of Fig. 4 shows the filtered $\Psi_4^{\ell=2,m=0}$ from CCM at the highest resolution. The time axis has been adjusted such that the peak of the original $\Psi_4^{\ell=2,m=0}$ occurs at $u = 0$. We first confirm that, after the QNM regime ($u \gtrsim 160M$), the filtered data accurately aligns with the raw $\Psi_4^{\ell=2,m=0}$ (green).

The filters extend the nonoscillatory regime. We find that the data within the window $u \in [50M, 400M]$ can be well fit by a single power law:

$$(u + 19.1)^{-3.79}. \quad (4)$$

To improve fitting performance, we borrow the spirit of

variable projection [48] by separating linear parameters from nonlinear ones. This step reduces a multidimensional fitting problem to a 1D problem. We have checked that the fit is highly stable against the initial guess. For more details, see the discussion around Eq. (73) in [49]. The bottom panel of Fig. 4 shows the fitted exponent for a window $[u_{\text{start}}, 400M]$, where u_{start} varies from $50M$ to $300M$. The window is capped at $400M$ to exclude numerical wiggles at later times. The obtained exponent remains stable around -3.8 for $u_{\text{start}} \in [50M, 200M]$. Beyond this range, the signal within the window is too inaccurate to determine the exponent.

The exponent differs from the Price law u^{-6} for $\Psi_4^{\ell=2, m=0}$ [50, 51]. We propose two possible origins of the tail:

- Intermediate regime of a linear tail. As shown in Fig. 4 of [52], the tail component requires $u > 10^4$ to fully converge to the Price law. At $u \gtrsim 100$, the exponent ranges from -3.5 to -4.2 (our exponent for Ψ_4 differs from the strain exponent in [52] by 2). Our extracted exponent falls within this range and shows a slight decrease over time, consistent with the behavior shown in Fig. 4 of [52].
- Source-driven “tail”. As discussed in [53, 54], an outgoing QNM generates a quadratic source that falls polynomially with distance. At second order, it yields a power-law decay in GWs, expected to follow u^{-4} in Ψ_4 [Eq. (66) in [53]²]. Since this decays slower than the Price law, the nonlinearity likely dominates at late times. The presence of the quadratic QNM $2\omega_{200}$ supports this possibility.

Both channels produce similar power laws in our window³. They can be distinguished by examining the tail behavior under different binary configurations, e.g., initial separation and orbital eccentricity. The quadratic channel might establish a determined link between the “tail” and the quadratic QNM, similar to the quadratic-to-linear ratios in [57, 58]. We leave this for future work.

Quasi-circular collision.— Our second case is a merger of two equal-mass, nonspinning BHs on a quasi-circular orbit. The orbital eccentricity is iteratively reduced to below $\sim 4 \times 10^{-4}$ [59–61]. The system undergoes ~ 12 orbits before the merger. The outer boundary is at a radius of $300M$ from the center of mass. The common horizon forms at $t = 2562.4M$. The remnant Kerr BH has a mass of $0.95149M$ and a dimensionless spin of 0.68641 . No instability is observed. Constraint violations

converge with numerical resolution. Plots can be found in the Supplementary Material.

Figure 5 compares $\Psi_4^{\ell=m=2}$ extracted with and without CCM. The difference between them is within the numerical error, and no tail is found. The result is consistent with the conclusion in [52]: backscattered waves (corrections from CCM) are suppressed in quasi-circular binaries.

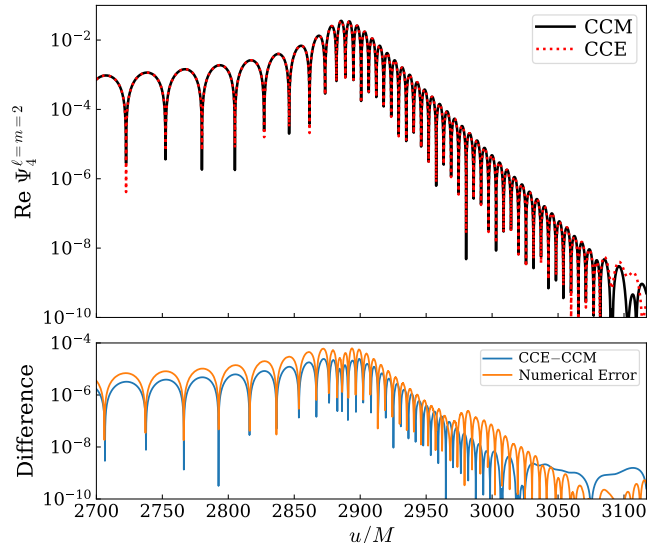


Figure 5. Top panel: $\Psi_4^{\ell=m=2}$ from a quasi-circular collision, simulated using CCM (black) and CCE (red). Bottom panel: The difference between the two results (blue), compared to the numerical error (orange).

Discussion.— We have successfully evolved BBH mergers on an effectively infinite computational domain using CCM. Both the head-on and quasi-circular systems were stable and convergent. In the head-on case, the CCM waveform agreed with that of a reference system with a distant outer boundary, whereas the CCE result exhibited a systematic error. A tail was identified in both the CCM and reference waveforms. By utilizing QNM rational filters, the tail within the window $u \in [50M, 400M]$ could be described by a power law. We proposed two possible origins for the phenomenon: either the intermediate regime of a linear tail or the source-driven nonlinear “tail” [53, 54]. In the quasi-circular system, no significant difference was observed between CCE and CCM.

Our simulations for the two extreme cases (orbital eccentricity = 0, 1) support the conclusion in [52, 62]: backscattered effects increase with orbital eccentricity. With CCM as an efficient method, a future avenue is to investigate tails in eccentric binaries, using the improved initial-data solver in [63].

We suggested the possible excitation of the source-driven “tail”. Comprehensive studies, including both theoretical insights and CCM numerical experiments with more BBH configurations, are essential for understanding

² The exact exponent may remain uncertain, as the authors found discrepancies between some numerical simulations and analytical predictions.

³ QNMs also produce power-law decays via other channels [55, 56].

the phenomenon. If confirmed as nonlinear, this would be an example where nonlinearity prevails over linearity at late times.

Acknowledgments.— S. M. would like to thank Luis Lehner, Conner Dailey, and Eric Poisson for useful discussions. Research at Perimeter Institute is supported in part by the Government of Canada through the Department of Innovation, Science and Economic Development and by the Province of Ontario through the Ministry of Colleges and Universities. This material is based upon work supported by the National Science Foundation under Grants No. PHY-2407742, No. PHY-2207342, and No. OAC-2209655 at Cornell. Any opinions, findings, and conclusions or recommendations expressed in this material are those of the author(s) and do not necessarily reflect the views of the National Science Foundation. This work was supported by the Sherman Fairchild Foundation at Cornell. This work was supported in part by the Sherman Fairchild Foundation and by NSF Grants No. PHY-2309211, No. PHY-2309231, and No. OAC-2209656 at Caltech. The computations presented here were conducted in the Resnick High Performance Computing Center, a facility supported by Resnick Sustainability Institute at the California Institute of Technology.

REFERENCES

- * sma2@perimeterinstitute.ca
- [1] E. W. Allen, E. Buckmiller, L. M. Burko, and R. H. Price, *Phys. Rev. D* **70**, 044038 (2004), arXiv:gr-qc/0401092.
 - [2] M. Dafermos and I. Rodnianski, (2004), arXiv:gr-qc/0403034.
 - [3] J. Winicour, *Living Reviews in Relativity* **15**, 1 (2012).
 - [4] C. Peterson, S. Gautam, A. Vañó Viñuales, and D. Hilditch, (2024), arXiv:2409.02994 [gr-qc].
 - [5] R. Panosso Macedo and A. Zenginoglu, (2024), arXiv:2409.11478 [gr-qc].
 - [6] F. Pretorius, *Phys. Rev. Lett.* **95**, 121101 (2005), arXiv:gr-qc/0507014 [gr-qc].
 - [7] M. Boyle *et al.*, *Class. Quant. Grav.* **36**, 195006 (2019), arXiv:1904.04831 [gr-qc].
 - [8] SXS Collaboration, “The SXS collaboration catalog of gravitational waveforms,” <http://www.black-holes.org/waveforms>.
 - [9] N. T. Bishop, in *Approaches to Numerical Relativity*, edited by R. D’Inverno (1992) pp. 20–33.
 - [10] N. T. Bishop, R. Gomez, L. Lehner, and J. Winicour, *Phys. Rev. D* **54**, 6153 (1996), arXiv:gr-qc/9705033 [gr-qc].
 - [11] N. T. Bishop, R. Gomez, L. Lehner, M. Maharaj, and J. Winicour, *Phys. Rev. D* **56**, 6298 (1997), arXiv:gr-qc/9708065.
 - [12] N. T. Bishop, R. Gomez, L. Lehner, B. Szilágyi, J. Winicour, and R. A. Isaacson, “Cauchy characteristic matching,” in *Black Holes, Gravitational Radiation and the Universe: Essays in Honor of C.V. Vishveshwara*, edited by B. R. Iyer and B. Bhawal (1998) pp. 383–408, arXiv:gr-qc/9801070.
 - [13] K. Barkett, J. Moxon, M. A. Scheel, and B. Szilágyi, *Phys. Rev. D* **102**, 024004 (2020), arXiv:1910.09677 [gr-qc].
 - [14] J. Moxon, M. A. Scheel, and S. A. Teukolsky, *Phys. Rev. D* **102**, 044052 (2020), arXiv:2007.01339 [gr-qc].
 - [15] J. Moxon, M. A. Scheel, S. A. Teukolsky, N. Deppe, N. Fischer, F. Hébert, L. E. Kidder, and W. Thrope, *Phys. Rev. D* **107**, 064013 (2023), arXiv:2110.08635 [gr-qc].
 - [16] C. Reisswig, N. T. Bishop, D. Pollney, and B. Szilágyi, *Phys. Rev. Lett.* **103**, 221101 (2009), arXiv:0907.2637 [gr-qc].
 - [17] K. Mitman *et al.*, *Class. Quant. Grav.* **41**, 223001 (2024), arXiv:2405.08868 [gr-qc].
 - [18] S. Ma *et al.*, *Phys. Rev. D* **109**, 124027 (2024), arXiv:2308.10361 [gr-qc].
 - [19] L. Lindblom, M. A. Scheel, L. E. Kidder, R. Owen, and O. Rinne, *Class. Quant. Grav.* **23**, S447 (2006), arXiv:gr-qc/0512093 [gr-qc].
 - [20] L. E. Kidder, L. Lindblom, M. A. Scheel, L. T. Buchman, and H. P. Pfeiffer, *Phys. Rev. D* **71**, 064020 (2005), arXiv:gr-qc/0412116 [gr-qc].
 - [21] L. T. Buchman and O. C. A. Sarbach, *Class. Quant. Grav.* **23**, 6709 (2006), arXiv:gr-qc/0608051.
 - [22] L. T. Buchman and O. C. A. Sarbach, *Class. Quant. Grav.* **24**, S307 (2007), arXiv:gr-qc/0703129.
 - [23] O. Rinne, L. T. Buchman, M. A. Scheel, and H. P. Pfeiffer, *Class. Quant. Grav.* **26**, 075009 (2009), arXiv:0811.3593 [gr-qc].
 - [24] L. T. Buchman, M. D. Duez, M. Morales, M. A. Scheel, T. M. Kosterlitz, A. M. Evans, and K. Mitman, *Class. Quant. Grav.* **41**, 175011 (2024), arXiv:2402.12544 [gr-qc].
 - [25] O. Rinne, *Class. Quant. Grav.* **23**, 6275 (2006), arXiv:gr-qc/0606053 [gr-qc].
 - [26] O. Rinne, L. Lindblom, and M. A. Scheel, *Class. Quant. Grav.* **24**, 4053 (2007), arXiv:0704.0782 [gr-qc].
 - [27] C. Dailey, E. Schnetter, and N. Afshordi, (2024), arXiv:2409.17970 [gr-qc].
 - [28] B. Szilágyi, L. Lindblom, and M. A. Scheel, *Phys. Rev. D* **80**, 124010 (2009), arXiv:0909.3557 [gr-qc].
 - [29] H. Bondi, M. G. J. van der Burg, and A. W. K. Metzner, *Proceedings of the Royal Society of London Series A* **269**, 21 (1962).
 - [30] R. K. Sachs, *Proceedings of the Royal Society of London. Series A. Mathematical and Physical Sciences* **270**, 103 (1962).
 - [31] B. Szilágyi, J. Blackman, A. Buonanno, A. Taracchini, H. P. Pfeiffer, M. A. Scheel, T. Chu, L. E. Kidder, and Y. Pan, *Phys. Rev. Lett.* **115**, 031102 (2015), arXiv:1502.04953 [gr-qc].
 - [32] N. Deppe, W. Thrope, L. E. Kidder, N. L. Vu, K. C. Nelli, *et al.*, “Spectre,” 10.5281/zenodo.10967177 (2024).
 - [33] G. Lovelace *et al.*, (2024), arXiv:2410.00265 [gr-qc].
 - [34] “The Spectral Einstein Code,” <http://www.black-holes.org/SpEC.html>.
 - [35] B. Szilágyi, *Int. J. Mod. Phys. D* **23**, 1430014 (2014), arXiv:1405.3693 [gr-qc].
 - [36] J. W. York, Jr., *Phys. Rev. Lett.* **82**, 1350 (1999), arXiv:gr-qc/9810051 [gr-qc].
 - [37] H. P. Pfeiffer and J. W. York, Jr., *Phys. Rev. D* **67**, 044022 (2003), arXiv:gr-qc/0207095 [gr-qc].
 - [38] H. P. Pfeiffer, *J. Hyperbol. Diff. Equat.* **2**, 497 (2005), arXiv:gr-qc/0412002.
 - [39] V. Varma, M. A. Scheel, and H. P. Pfeiffer, *Phys. Rev. D* **98**, 104011 (2018), arXiv:1808.08228 [gr-qc].

- [40] A. Ashtekar, T. De Lorenzo, and N. Khera, *Gen. Rel. Grav.* **52**, 107 (2020), arXiv:1906.00913 [gr-qc].
- [41] D. A. B. Iozzo, M. Boyle, N. Deppe, J. Moxon, M. A. Scheel, L. E. Kidder, H. P. Pfeiffer, and S. A. Teukolsky, *Phys. Rev. D* **103**, 024039 (2021), arXiv:2010.15200 [gr-qc].
- [42] M. Boyle, *Phys. Rev.* **D93**, 084031 (2016), arXiv:1509.00862 [gr-qc].
- [43] S. Ma, K. Mitman, L. Sun, N. Deppe, F. Hébert, L. E. Kidder, J. Moxon, W. Throwe, N. L. Vu, and Y. Chen, *Phys. Rev. D* **106**, 084036 (2022), arXiv:2207.10870 [gr-qc].
- [44] S. Ma, L. Sun, and Y. Chen, *Phys. Rev. Lett.* **130**, 141401 (2023), arXiv:2301.06705 [gr-qc].
- [45] S. Ma, L. Sun, and Y. Chen, *Phys. Rev. D* **107**, 084010 (2023), arXiv:2301.06639 [gr-qc].
- [46] https://github.com/Sizheng-Ma/qnm_filter.
- [47] T. May, S. Ma, J. L. Ripley, and W. E. East, *Phys. Rev. D* **110**, 084034 (2024), arXiv:2405.18303 [gr-qc].
- [48] D. P. O’Leary and B. W. Rust, *Computational Optimization and Applications* **54**, 579 (2013).
- [49] S. Ma, K. C. Nelli, J. Moxon, M. A. Scheel, N. Deppe, L. E. Kidder, W. Throwe, and N. L. Vu, (2024), arXiv:2409.06141 [gr-qc].
- [50] R. H. Price, *Phys. Rev. D* **5**, 2419 (1972).
- [51] E. W. Leaver, *Phys. Rev. D* **34**, 384 (1986).
- [52] M. De Amicis, S. Albanesi, and G. Carullo, *Phys. Rev. D* **110**, 104005 (2024), arXiv:2406.17018 [gr-qc].
- [53] V. Cardoso, G. Carullo, M. De Amicis, F. Duque, T. Katagiri, D. Pereniguez, J. Redondo-Yuste, T. F. M. Spieksma, and Z. Zhong, *Phys. Rev. D* **109**, L121502 (2024), arXiv:2405.12290 [gr-qc].
- [54] S. Okuzumi, K. Ioka, and M.-a. Sakagami, *Phys. Rev. D* **77**, 124018 (2008), arXiv:0803.0501 [gr-qc].
- [55] S. R. Green, F. Carrasco, and L. Lehner, *Phys. Rev. X* **4**, 011001 (2014), arXiv:1309.7940 [hep-th].
- [56] H. Yang, A. Zimmerman, A. Zenginoğlu, F. Zhang, E. Berti, and Y. Chen, *Phys. Rev. D* **88**, 044047 (2013), arXiv:1307.8086 [gr-qc].
- [57] N. Khera, S. Ma, and H. Yang, (2024), arXiv:2410.14529 [gr-qc].
- [58] S. Ma and H. Yang, *Phys. Rev. D* **109**, 104070 (2024), arXiv:2401.15516 [gr-qc].
- [59] H. P. Pfeiffer, D. A. Brown, L. E. Kidder, L. Lindblom, G. Lovelace, and M. A. Scheel, *New frontiers in numerical relativity. Proceedings, International Meeting, NFNR 2006, Potsdam, Germany, July 17-21, 2006*, *Class. Quant. Grav.* **24**, S59 (2007), arXiv:gr-qc/0702106 [gr-qc].
- [60] A. Buonanno, L. E. Kidder, A. H. Mroue, H. P. Pfeiffer, and A. Taracchini, *Phys. Rev.* **D83**, 104034 (2011), arXiv:1012.1549 [gr-qc].
- [61] A. H. Mroue and H. P. Pfeiffer, (2012), arXiv:1210.2958 [gr-qc].
- [62] T. Islam, G. Faggioli, G. Khanna, S. E. Field, M. van de Meent, and A. Buonanno, (2024), arXiv:2407.04682 [gr-qc].
- [63] T. Knapp, K. Chatziioannou, H. Pfeiffer, M. A. Scheel, and L. E. Kidder, (2024), arXiv:2410.02997 [gr-qc].
- [64] https://spectre-code.org/structCce_1_1InitializeJ_1_1ConformalFactor.html.
- [65] N. Bishop, D. Pollney, and C. Reisswig, *Class. Quant. Grav.* **28**, 155019 (2011), arXiv:1101.5492 [gr-qc].
- [66] E. E. Flanagan and D. A. Nichols, *Phys. Rev. D* **95**, 044002 (2017), [Erratum: *Phys.Rev.D* 108, 069902 (2023)], arXiv:1510.03386 [hep-th].
- [67] K. Mitman, J. Moxon, M. A. Scheel, S. A. Teukolsky, M. Boyle, N. Deppe, L. E. Kidder, and W. Throwe, *Phys. Rev. D* **102**, 104007 (2020), arXiv:2007.11562 [gr-qc].

SUPPLEMENTAL MATERIAL

The characteristic initial data

Currently, `SpECTRE` supports various options for constructing characteristic initial data empirically. Although, in principle, the initial data should be *uniquely* determined from an *ab initio* approach, the default method known as `ConformalFactor` [64] in `SpECTRE` has proven to be a suitable choice [17]. In particular, it can help reduce initial junk radiation in the memory modes of BBH systems (see discussions below). Providing a comprehensive discussion on how characteristic initial data affects GW waveforms [65] and developing an *ab initio* initial-data solver is beyond the scope of this paper. Here we give a brief summary of the `ConformalFactor` method, as it was not fully explained in [15].

The `SpECTRE` characteristic system evolves two scalars and a vector, including

- Bondi J : This complex scalar is a volume variable that depends on both angular and radial coordinates. Its evolution is governed by a hierarchical system, see e.g., Eqs. (14)–(18) in [13].
- Cauchy angular coordinates $x^A = (\theta, \phi)$: These coordinates form a real vector defined on an extraction worldtube, usually chosen to be a sphere. Cauchy’s angular coordinates do not align with those of the characteristic system — they evolve over time with respect to the characteristic coordinates. The evolution equation can be found in Eq. (4.53) of [18]. This time-dependent mapping between the two coordinate systems is crucial for variable interpolation on the worldtube.
- Bondi time \hat{u} : The `SpECTRE` characteristic system adopts the so-called partially flat Bondi-like coordinates, see Table I in [14] and Fig. 1 in [18], whose time coordinate differs from the true Bondi time. The two time coordinates are related via $\hat{u} = \int e^{2\beta} du + \hat{u}^{(R)}$, see Eq. (35) in [14] for more details. The mapping can be interpreted as a BMS transformation: the term involving $e^{2\beta}$ yields time dilation via the conformal factor ω in Eq. (2.12a) of [66], while $\hat{u}^{(R)}$ contributes to a supertranslation. Waveform quantities are asymptotically transformed into the true Bondi frame only at the output stage. The BMS transformations for these waveform quantities can be found in Eq. (94) of [14], consistent with Eq. (17) of [42].

Initial data are needed for all of these evolved variables.

For the Bondi time \hat{u} , its initial data sets the angular-dependent integration constant for $\hat{u} = \int e^{2\beta} du$, which reflects the supertranslation freedom of the first characteristic slice. Currently, the constant is hard-coded to zero in `SpECTRE`.

The initialization of J is based on the cubic ansatz, see Eq. (16) of [15]

$$J = \frac{A}{r} + \frac{B}{r^3}. \quad (5)$$

The coefficients A and B are determined by the worldtube data for J and $\partial_r J$ taken from a Cauchy evolution. Here the term $1/r^2$ is omitted to avoid logarithmic terms, see Sec. V B of [14].

The initial data for the Cauchy angular coordinates x^A deserves more attention. Denoting the characteristic angular coordinates as $\hat{x}^{\hat{A}}$, the mapping between them is controlled by the Jacobian $\partial_{\hat{A}} x^A$. In `SpECTRE`, the Jacobian is represented by two complex scalars $\hat{a} = \hat{q}^{\hat{A}} \partial_{\hat{A}} x^A q_A$ and $\hat{b} = \hat{\bar{q}}^{\hat{A}} \partial_{\hat{A}} x^A q_A$ [see Eq. (4.13) of [18]]

$$\partial_{\hat{A}} x^A = \frac{1}{4} \begin{pmatrix} \hat{q}_{\hat{A}} & \hat{\bar{q}}_{\hat{A}} \\ \hat{\bar{b}} & \hat{a} \end{pmatrix} \begin{pmatrix} q^A \\ \bar{q}^A \end{pmatrix}, \quad (6)$$

where the dyad q^A is given by $(-1, -i \csc \theta)$. Treating the Jacobian as a 2×2 matrix, its determinant $\hat{\omega}$ can be computed via

$$\hat{\omega}^2 = \frac{1}{2} \epsilon_{AB} \epsilon^{\hat{A}\hat{B}} \partial_{\hat{A}} x^A \partial_{\hat{B}} x^B = \frac{1}{4} (\hat{b}\bar{\hat{b}} - \hat{a}\bar{\hat{a}}), \quad (7)$$

where $\epsilon_{AB} = \frac{i}{2} q_A \wedge \bar{q}_B$ is the volume form compatible with the unit sphere metric. To obtain Eq. (7), we have used $q^A \epsilon_{AB} = -i q_B$.

Similar to BMS symmetries, where a conformal isometry of the 2-sphere leads to time dilation, see Eq. (2.12a) of [66], the angular diffeomorphism in the present case also leads to the transformation of the Bondi β [Eq. (33a) of [14]]

$$e^{2\hat{\beta}} = e^{2\beta} / \hat{\omega}, \quad (8)$$

where the value of β on a worldtube comes from a Cauchy evolution, and the transformed $\hat{\beta}$ is defined in the partially flat Bondi-like coordinates, used for future hypersurface integration. `SpECTRE` now sets the initial value of $\hat{\beta}$ to zero, which yields an algebraic equation for the Jacobian:

$$e^{2\beta} = \hat{\omega} = \frac{1}{2} \sqrt{\hat{b}\hat{b} - \hat{a}\hat{a}}. \quad (9)$$

where we have used Eq. (7). Since the determinant $\hat{\omega}$ plays a similar role as the conformal factor in BMS, this method is thus termed `ConformalFactor`. In the code, Eq. (9) is iteratively inverted to solve for the scalars \hat{a} and \hat{b} , thereby constructing $x^A(\hat{x}^{\hat{A}})$. Roughly speaking, Eq. (9) sets the initial “lapse” at the worldtube to unity, aligning the clock rate with that of inertial observers at future null infinity.

The initial condition for $x^A(\hat{x}^{\hat{A}})$ is crucial in reducing the junk radiation in memory modes, see the red curve in Fig. 10 of [67]. There, a less motivated initial condition $\hat{x}^{\hat{A}} = \delta_A^{\hat{A}} x^A$ was used⁴.

Additional plots for the quasi-circular binary

This section provides additional plots for the quasi-circular binary. Figure 6 displays the L^2 -norm of the Cauchy GH constraint energy at three resolutions. The constraint violation converges with numerical resolution and finally stabilizes.

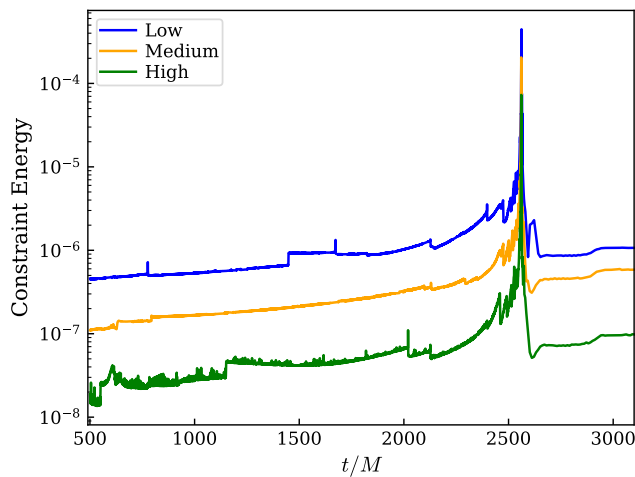


Figure 6. The L^2 -norm of the Cauchy GH constraint energy at three resolutions, for the quasi-circular binary simulated with CCM. The Cauchy time is used as the x -axis. The spike at $t = 2562.4M$ is expected and is when the system undergoes merger.

At future null infinity, Einstein’s equations and the Bianchi identities establish constraints across various waveform quantities, which read [40, 41]

$$C_{\Psi_4} \equiv \Psi_4 + \ddot{h}, \quad (10a)$$

$$C_{\Psi_3} \equiv \dot{\Psi}_3 + \frac{1}{2} \bar{\delta} \Psi_4, \quad (10b)$$

$$C_{\Psi_2} \equiv \dot{\Psi}_2 + \frac{1}{2} \bar{\delta} \Psi_3 - \frac{1}{4} \bar{h} \Psi_4, \quad (10c)$$

$$C_{\Psi_1} \equiv \dot{\Psi}_1 + \frac{1}{2} \bar{\delta} \Psi_2 - \frac{1}{2} \bar{h} \Psi_3, \quad (10d)$$

$$C_{\Psi_0} \equiv \dot{\Psi}_0 + \frac{1}{2} \bar{\delta} \Psi_1 - \frac{3}{4} \bar{h} \Psi_2, \quad (10e)$$

$$C_{\text{Im}\Psi_2} \equiv \text{Im} \left(\Psi_2 + \frac{1}{4} \bar{\delta}^2 h + \frac{1}{4} \dot{h} \bar{h} \right). \quad (10f)$$

⁴ The Bondi J was still constructed using Eq. (5).

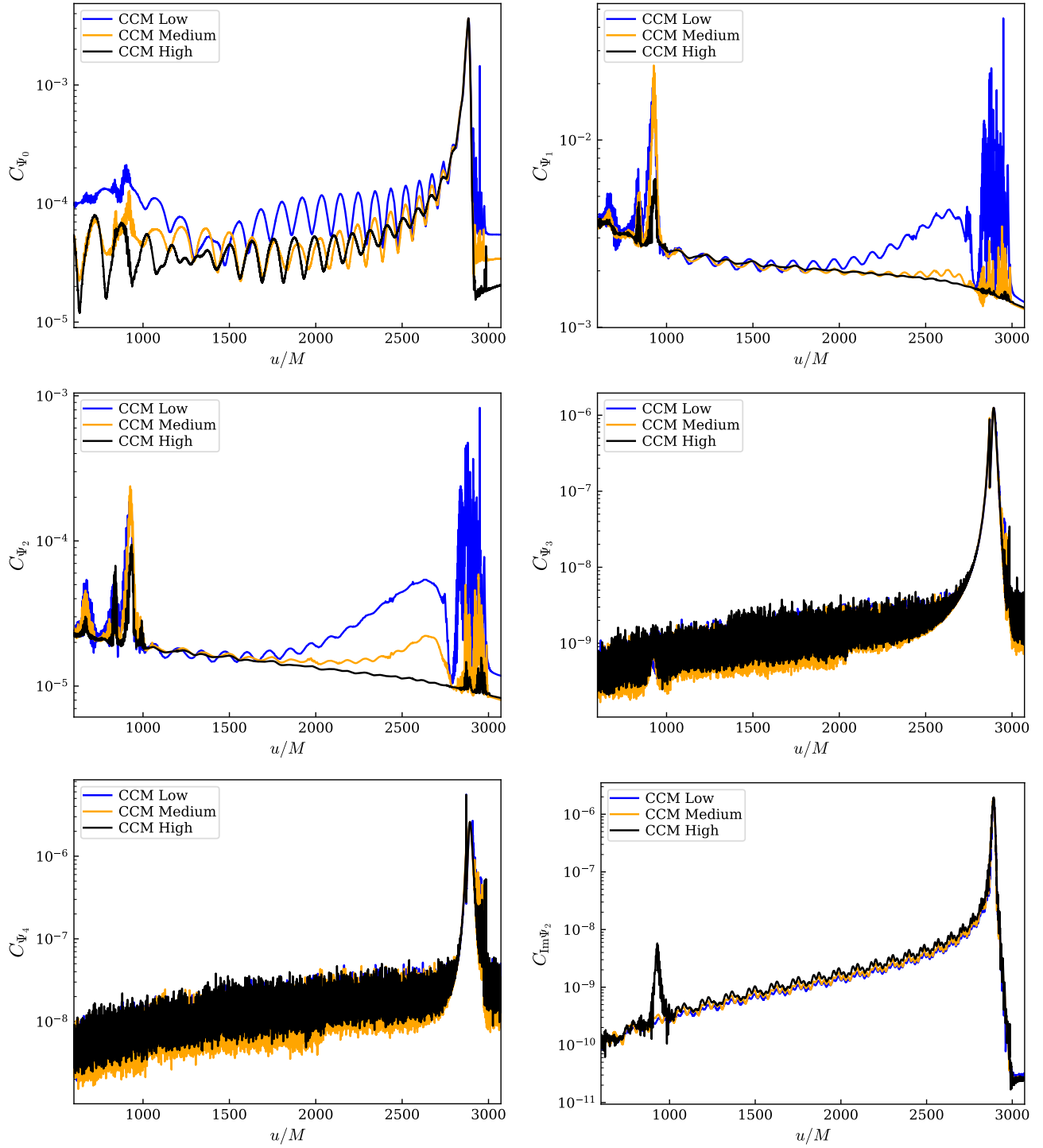


Figure 7. The L^2 -norm of the violations in the Bianchi identities, for the quasi-circular binary simulated with CCM. The retarded time is used as the x -axis.

Figure 7 shows the L^2 -norm of these constraint violations. They typically decrease as the numerical resolution improves, except for those already at the level of 10^{-6} . In this case, the violations with and without CCM are comparable, so only the results with CCM are shown.

Additional plots for the head-on collision

Figure 8 shows the L^2 -norm of the violations in the Bianchi identities [Eq. (10)], with CCM (solid curves) and without CCM (dotted curves). We can see that CCM systematically reduces the violations, except for those already at the level of 10^{-6} . In addition, the CCM results exhibit better convergence behavior.

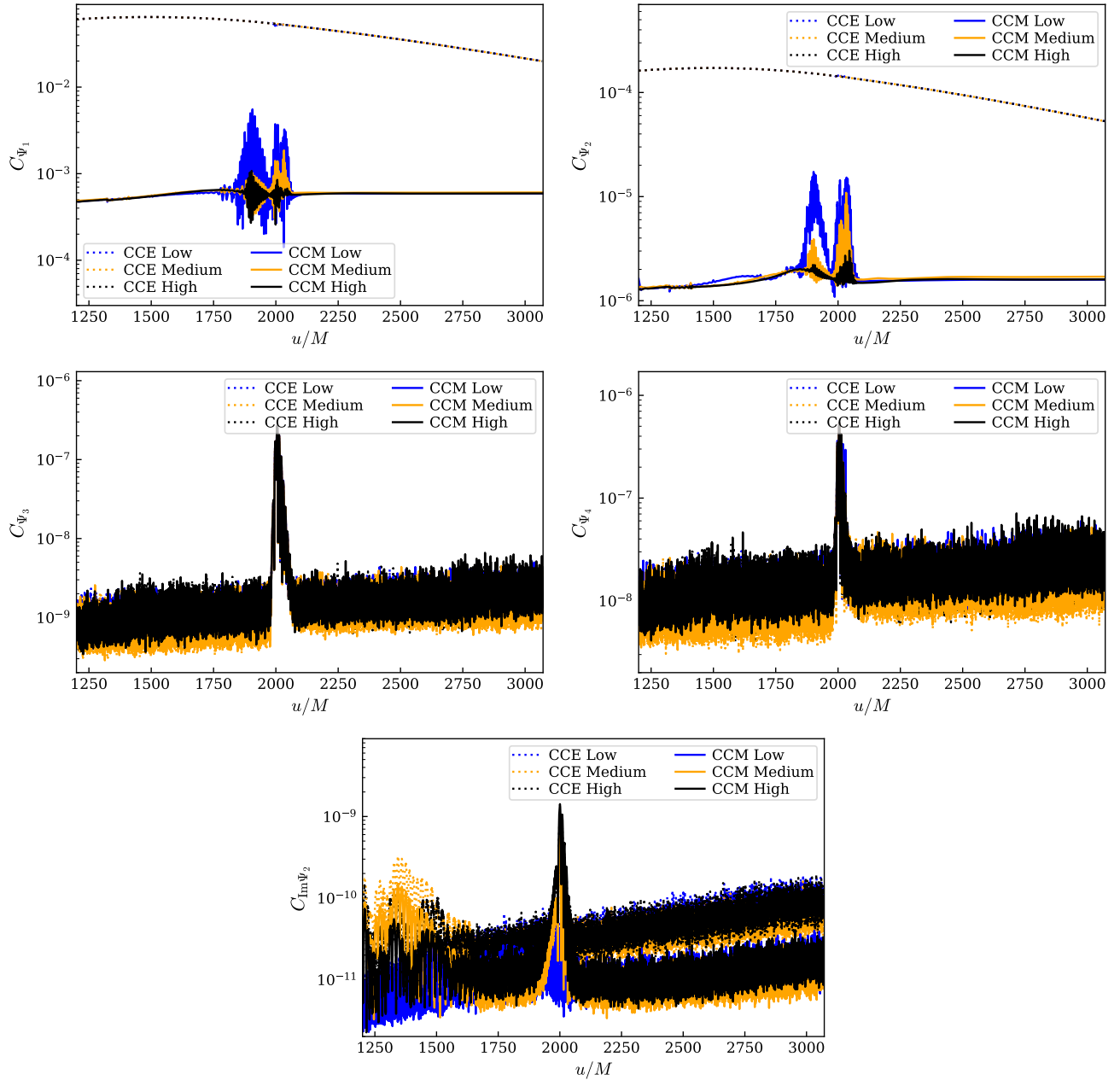


Figure 8. The L^2 -norm of the violations in the Bianchi identities for the head-on collision, simulated with CCM (solid curves) and without CCM (dotted curves). The retarded time is used as the x -axis.